Supplementary Materials for

In-situ Reactive Self-Assembly of Graphene Oxide Nano-Coating in Polymer Foam Materials with Synergistic Fire Shielding Properties

Yang Li,†[a] Cheng-Fei Cao,†[a] Shi-Neng Li,†[a] Neng-Jian Huang,[a] Min Mao,[a] Jian-Wang Zhang,[a] Peng-Huan Wang,[a] Kun-Yu Guo,[a] Li-Xiu Gong,[a] Guo-Dong Zhang,[a] Li Zhao,[a] Li-Zhi Guan,[b] Yan-Jun Wan,[c] Long-Cheng Tan[a] and Yiu-Wing Mai [d]*

[a] Key Laboratory of Organosilicon Chemistry and Material Technology of Ministry of Education, Hangzhou Normal University, Hangzhou 311121, China

[b] Instituto de Ciencia de Materiales de Madrid-ICMM, Consejo Superior de Investigaciones Cientificas-CSIC, Campus de Cantoblanco, 28049 Madrid, Spain

[c] Department of Mechanical and Automation Engineering, The Chinese University of Hong Kong, Shatin, NT, Hong Kong, China

[d] Centre for Advanced Materials Technology (CAMT), School of Aerospace, Mechanical and Mechatronic Engineering J07, The University of Sydney, Sydney, NSW, 2006, Australia

This PDF file includes:

Supplementary text

Critical content (X_C) of GO covered on the foam surface, Figure 2h

We calculate the critical content (X_C) of the GO sheets that are well covered on the entire foam surface based on the surface area values of porous SiRF and GO sheets. According to the average pore size distribution of SiRF shown in Fig. S6, we can calculate the average cell size (R_a) and volume of the cell (V_{cell}). Then, the total volume ($V_{t\text{-}cell}$) of all the cells is given by $n_{cell}V_{cell}$, where n_{cell} is the total number of cells. Thus, the total volume ($V_{t\text{-}c}$) of SiRF-GO nanocomposite can be obtained by:

$$V_{t\text{-}c} = V_{t\text{-}cell} + V_m \quad (1)$$

where V_m is the volume of the polymer matrix in the SiRF-GO nanocomposites. In fact, the density (ρ_c) of SiRF-GO nanocomposites can be calculated from:

$$\rho_c = m_{t\text{-}c}/V_{t\text{-}c} = \rho_m V_m/(V_{t\text{-}cell}+V_m) \quad (2)$$

where ρ_m is matrix density. The effect of the assembled GO sheets on the matrix density is not considered due to their low content used in this study.

The total surface area (S_{total}) of the SiRF-GO nanocomposites is given by:

$$S_{total} = (4\pi R_a^2)\, n_{cell} = (4\pi R_a^2)V_{t\text{-}cell}/V_{cell} = (4\pi R_a^2)V_{t\text{-}cell}/(4\pi R_a^3/3) = 3V_{t\text{-}cell}/R_a \quad (3)$$

Combining equations (2) and (3) yields:

$$S_{total} = 3V_m\,(\rho_m/\rho_c - 1)/R_a \quad (4)$$

The total surface area of GO sheets ($S_{t\text{-}GO}$) in the SiRF-GO nanocomposite becomes:

$$S_{t\text{-}GO} = n_{GO}S_{GO} = n_{GO}m_{GO}/(\rho_{GO}t_{GO}) = (m_{t\text{-}GO}/m_{GO})m_{GO}/(\rho_{GO}t_{GO}) = m_{t\text{-}GO}/(\rho_{GO}t_{GO}) \quad (5)$$

where n_{GO} and S_{GO} indicate the number and surface area of the GO sheet; ρ_{GO} and t_{GO} are the GO sheet density and thickness.

Considering the total mass of GO sheets ($m_{t\text{-}GO}$) in the SiRF-GO nanocomposites can be obtained by: $m_{t\text{-}GO} = V_m\rho_m X_{GO}$, where X_{GO} is the weight content of GO used in the SiRF-GO nanocomposites. Thus, the total surface area of GO sheets ($S_{t\text{-}GO}$) is given by:

$$S_{t\text{-}GO} = (V_m\rho_m X_{GO})/(\rho_{GO}t_{GO}) \quad (6)$$

The critical content of GO sheets (X_C) that cover the entire skeleton surface suggests that $S_{t\text{-}GO} = S_{total}$. Hence, X_C can be deduced from equations (4) and (6) which give:

$$X_C = 3\rho_{GO}t_{GO}(1/\rho_c - 1/\rho_m)/R_a \quad (7)$$

Based on the experimental results obtained in this study and previous literature [1], ρ_{GO}=1.32 g cm^{-3}, t_{GO}=1.0 nm, and R_a is ~226 µm for SiRF-GO nanocomposites with 0.10 wt% GO. ρ_c and ρ_m

are measured before/after the foaming process, which is 0.23 and 0.89 g cm^{-3}, respectively. As a result, the above simple model yields a theoretical X_C value of ~0.006 wt.% for SiRF. Considering the fact that the stacked and overlapped sheets are inevitably occurred in the GO/water solution at high GO concentration of ~20 mg mL^{-1}, the effective value of t_{GO} may be thicker than the fully exfoliated sheets observed at low concentration of 0.25 mg mL^{-1}. When the t_{GO} value is assumed to be 2-3 nm, the theoretical X_C value for SiRF are 0.01-0.02 wt.%.

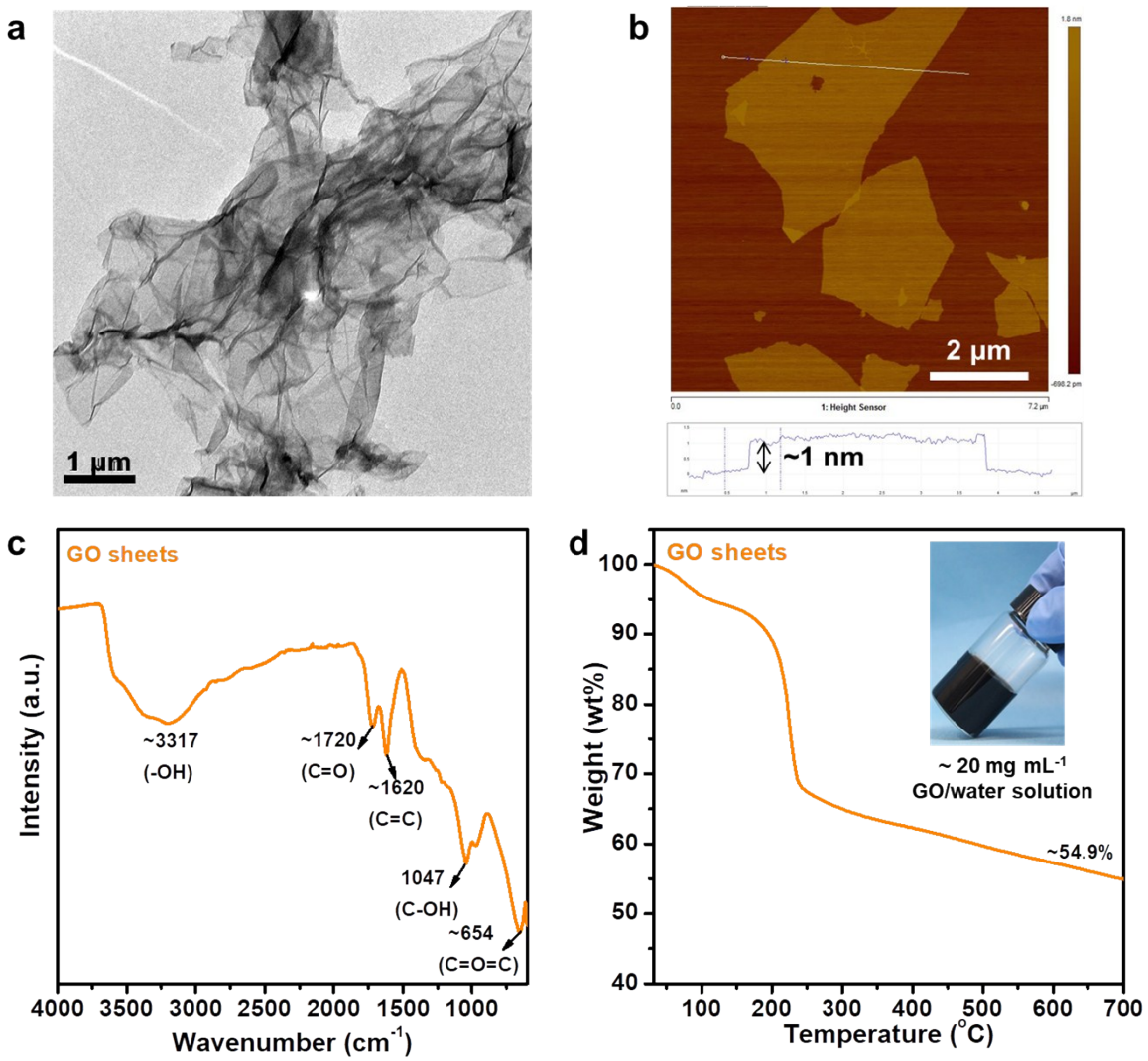

Fig. S1. Morphology and structure characterization of GO sheets. (a) SEM image of typical GO sheets, showing wrinkled structures and stacked phenomenon due to the complicated interactions among the sheets. (b) A typical AFM image of GO sheets (GO/water concentration of ~0.25 mg mL^{-1}) with lateral size ranging from 1-10 μm. The height difference between the steps is ~1.0 nm, indicating the typical height of a single layer GO sheet. (c) FTIR spectrum and (d) TGA curves of GO sheets, showing many oxygen groups on GO sheets. Inset displays GO sheets in aqueous solution at ~20 mg mL^{-1}, indicating a solid-like viscous state due to strong interactions among the GO sheets.

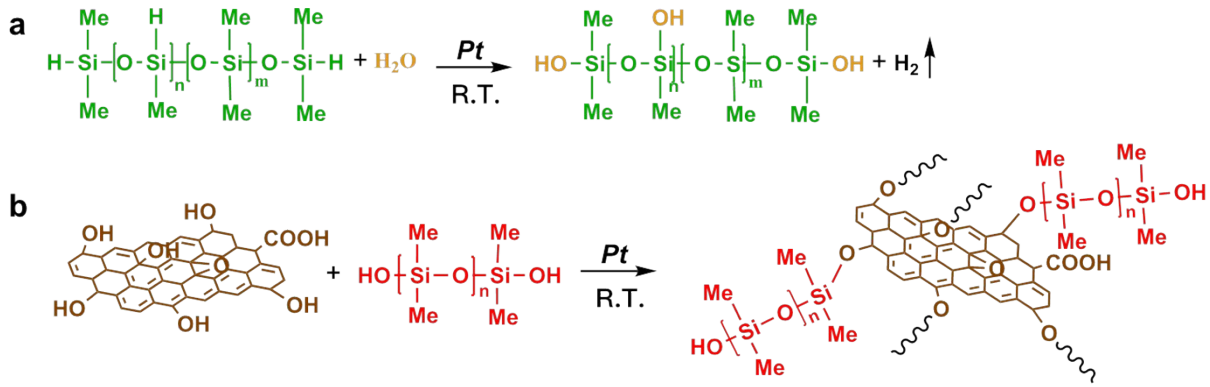

Fig. S2. Schematic of possible cross-linking/foaming reactions during synthesis of SiRF-GO foam. (a) Foaming reaction between hydrogen dimethicone and water under Pt catalysis at ambient temperature. (b) Cross-linking reaction between hydrogen groups of GO sheets and dihydroxy PDMS.

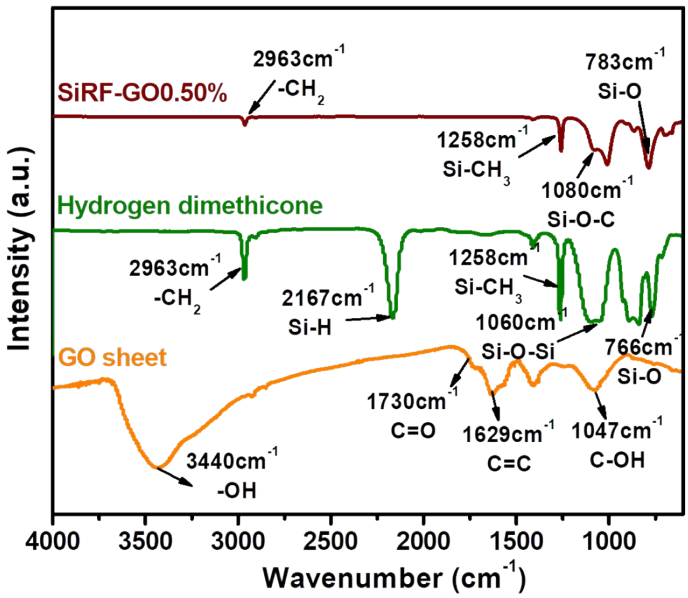

Fig. S3. FTIR results of GO sheets and hydrogen dimethicone and SiRF-GO0.50% nanocomposite after foaming. Compared with GO sheets and hydrogen dimethicone, the SiRF-GO0.50% nanocomposite shows disappearance of O-H at ~3440 cm^{-1} and C-OH at 1047 cm^{-1}, as well as the appearance of Si-O-C at ~1080 cm^{-1}, suggesting successful reaction between hydrogen dimethicone and GO sheets.

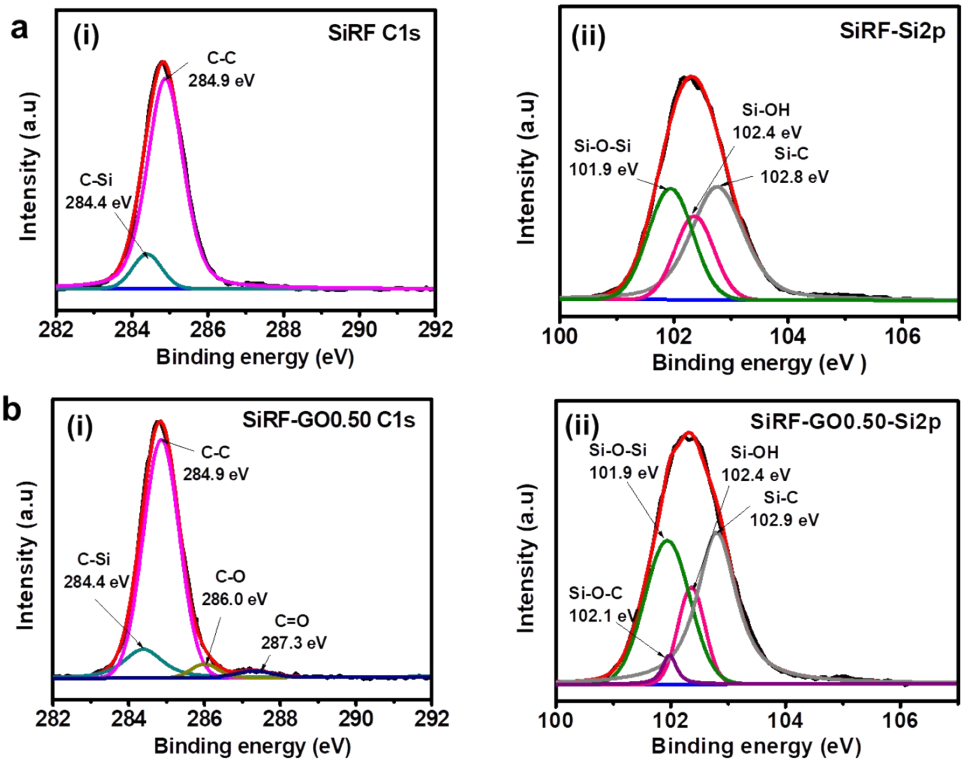

Fig. S4. XPS results of pure SiRF and SiRF-GO0.50%. C1s and Si2p spectra of (a) pure SiRF and (b) SiRF-GO, respectively, demonstrating the formation of C-O, C=O and Si-O-C due to chemical bonding between GO and silicone molecules.

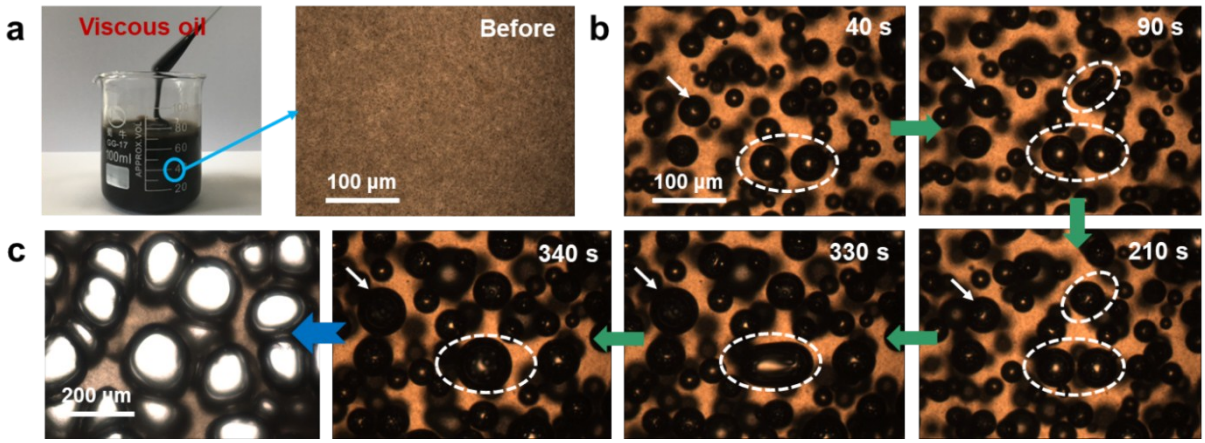

Fig. S5. (a) Digital and optical microscopy images of PDMS matrix containing about 0.25% GO sheets, and (b) typical optical microscopy images of foaming process of the above mixture at ambient temperature in 340 s. Transparent silicone phase and black GO-based suspension are visible, and the bubbles show size growth and integration as observed in other composition, which is consistent with the results in Fig. 1d. (c) Optical microscopy image of SiRF-GO0.25% samples, showing a typical porous structure.

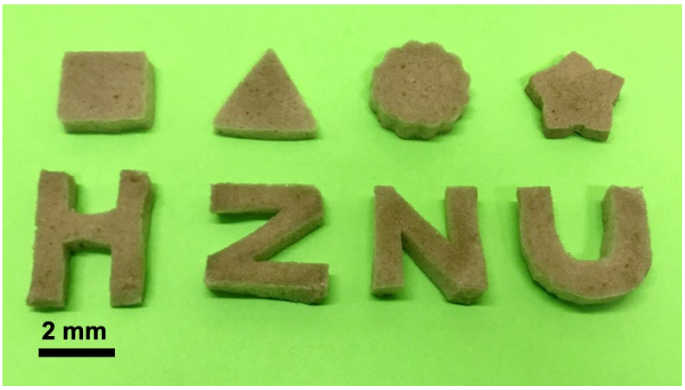

Fig. S6. Typical digital image of SiRF-GO0.25% samples, which can be cut into any desired shape.

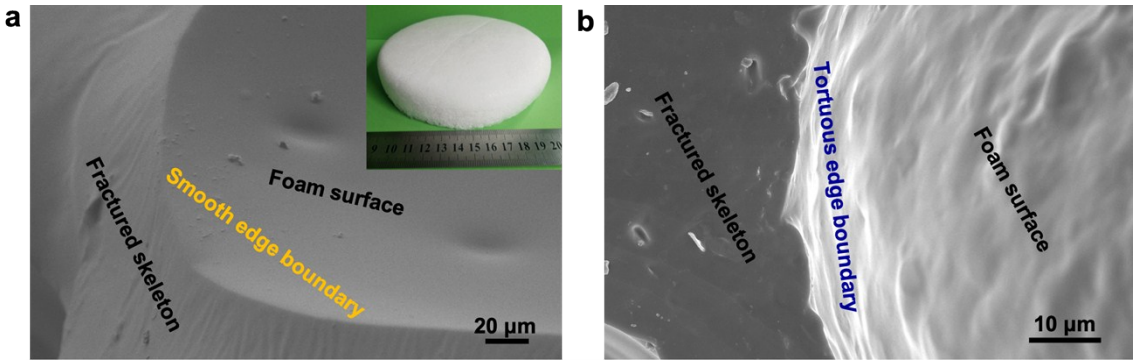

Fig. S7. Typical SEM images of (a) pure SiRF (inset: digital image of pure SiRF) and (b) SiRF-GO0.10%. White pure SiRF shows a smooth edge boundary and foam surface; while SiRF-GO0.10% displays a tortuous edge boundary, which would be due to the mono- or multi- GO sheets that are bonded with PDMS molecules assembled on the foam surface.

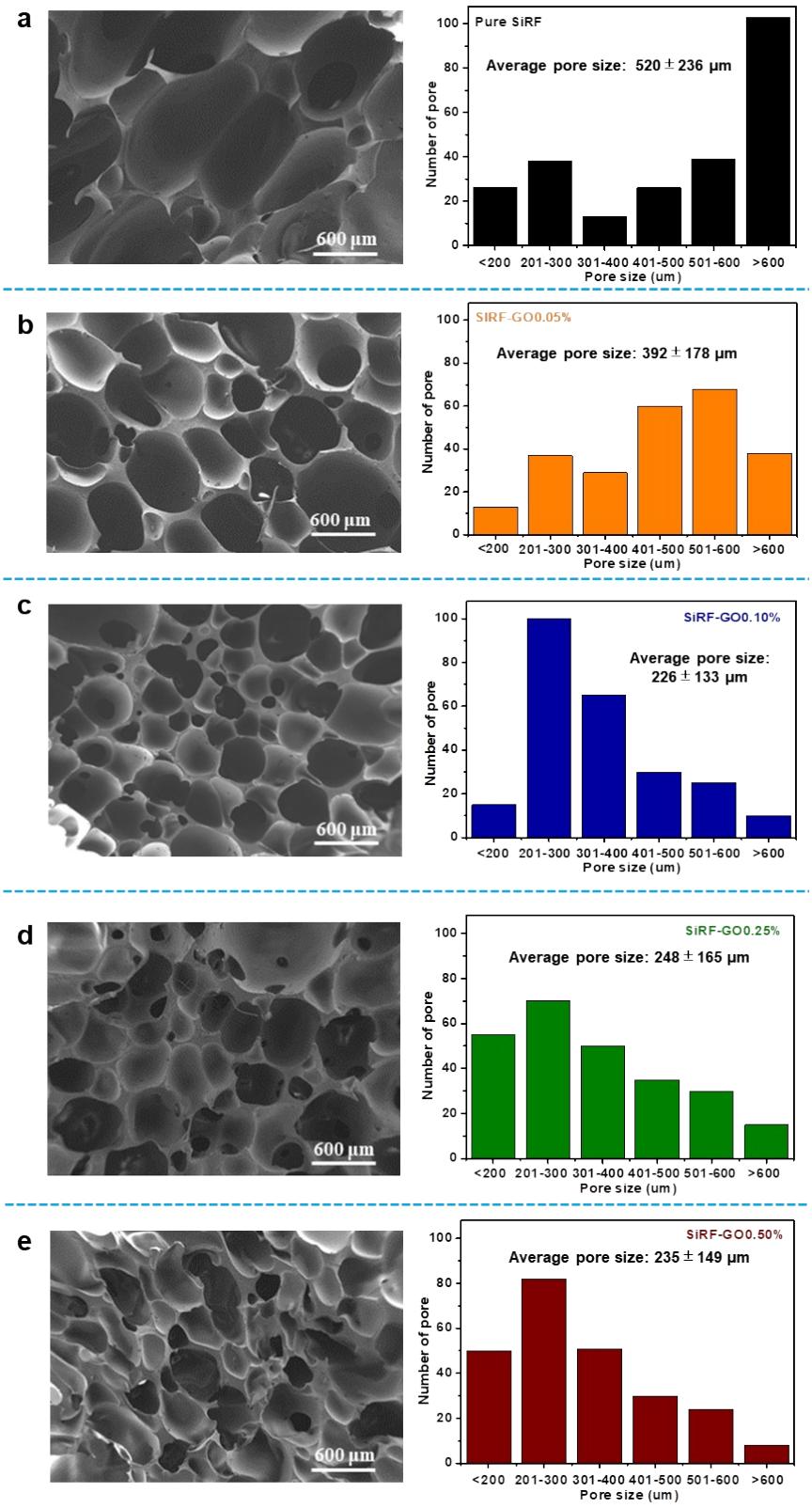

Fig. S8. Pore size analyses of pure SiRF and SiRF-GO composites. SEM fractographs and distributions of pore size for different samples: (a) pure SiRF, (b) SiRF-GO0.05%, (c) SiRF-GO0.10%, (d) SiRF-GO0.25%, and (e) SiRF-GO0.50%. Pore size shows slight reduction with addition of GO but retains almost the same size distribution for ≥ 0.10 wt.% GO.

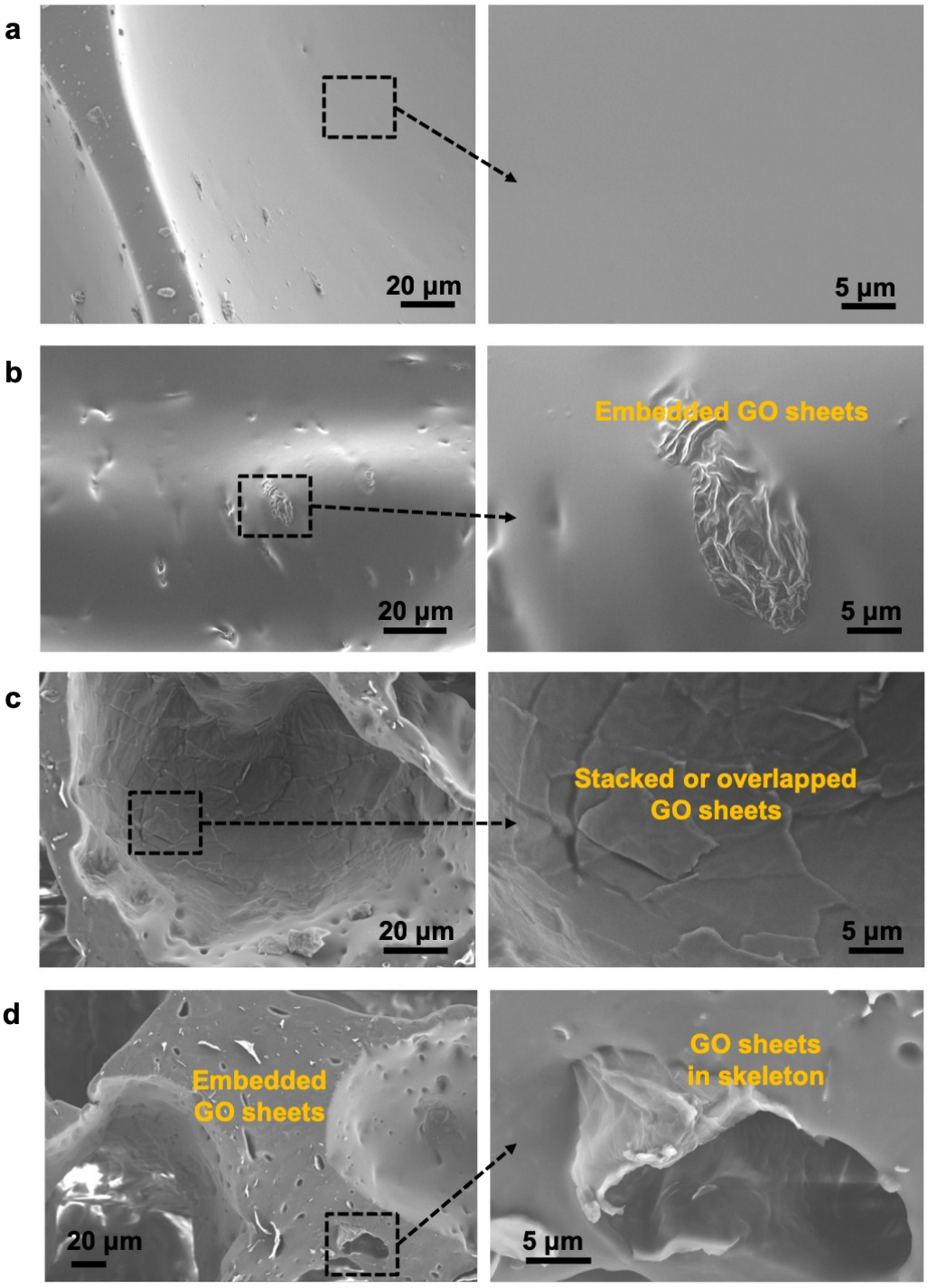

Fig. S9. SEM images of (a) pure SiRF and different SiRF-GO samples: (b) SiRF-GO0.05% and (c, d) SiRF-GO0.50%. Compared with the smooth surface of pure SiRF, SiRF nano-composites show much rougher surfaces. At low contents, GO sheets do not cover well the foam surface which shows some cluster structures. At high contents, GO sheets can cover the entire surface well, and some stacked GO sheets are found on the skeleton. In addition, some GO sheets are embedded within the matrix in the skeleton zone.

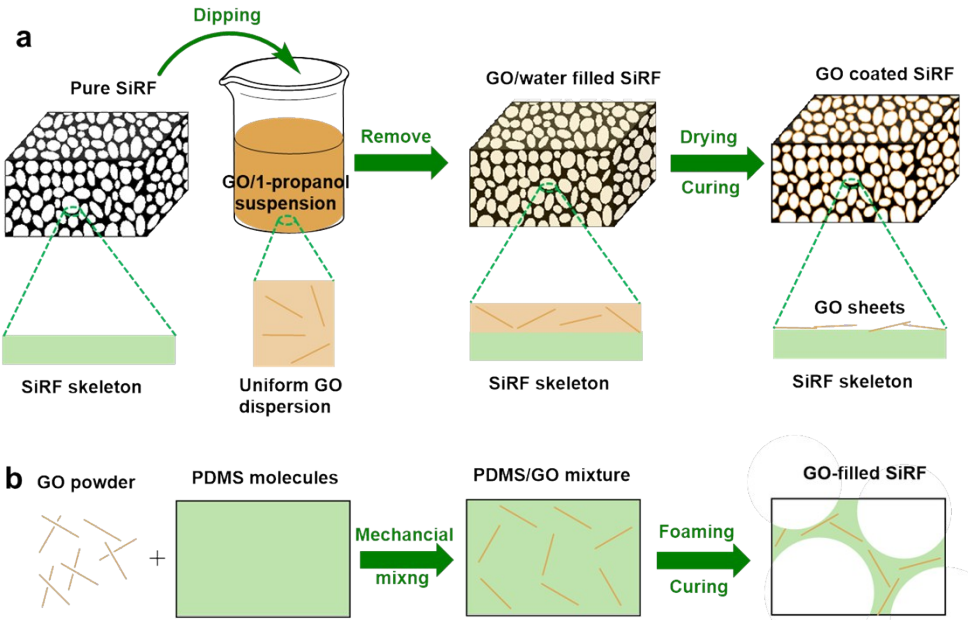

Fig. S10. Schematic of SiRF-GO nanocomposites by traditional fabrication processes. Preparation process of SiRF-GO nanocomposites by (a) a simple dip-coating (DC) method and (b) the mechanical mixing (MM) method.

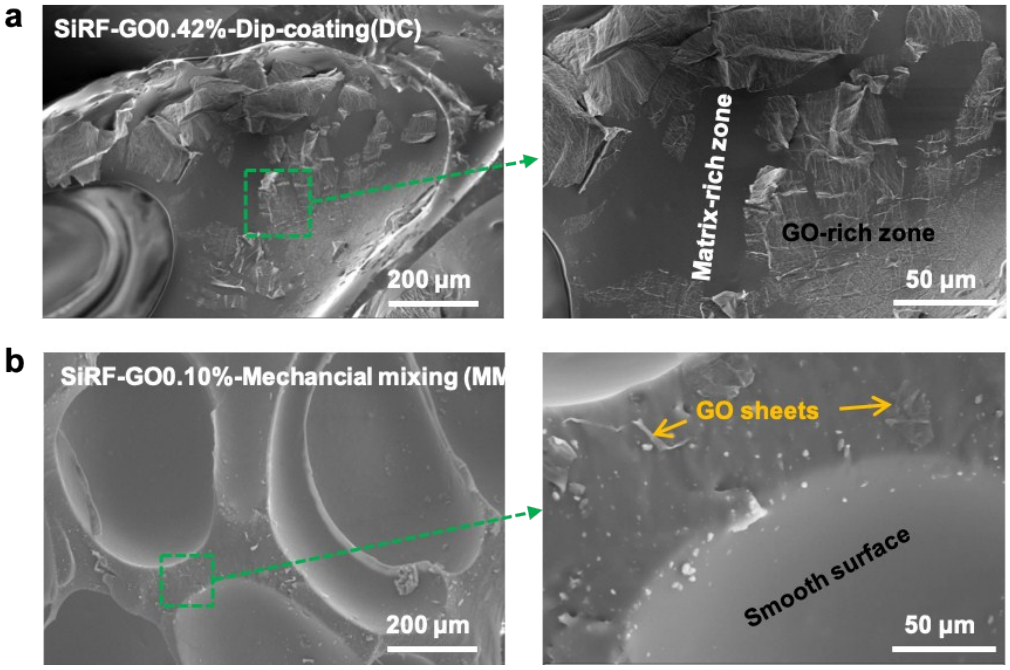

Fig. S11. SEM images of SiRF-GO nanocomposites fabricated by (a) Dip-Coating (DC) and (b) Mechanical Mixing (MM). SiRF-GO0.42%-DC shows that the GO sheets are not well distributed on the skeleton surface. For SiRF-GO0.10%-MM, the surface of the sample is smooth similar to that of pure SiRF and the GO sheets are well distributed on the foam surface.

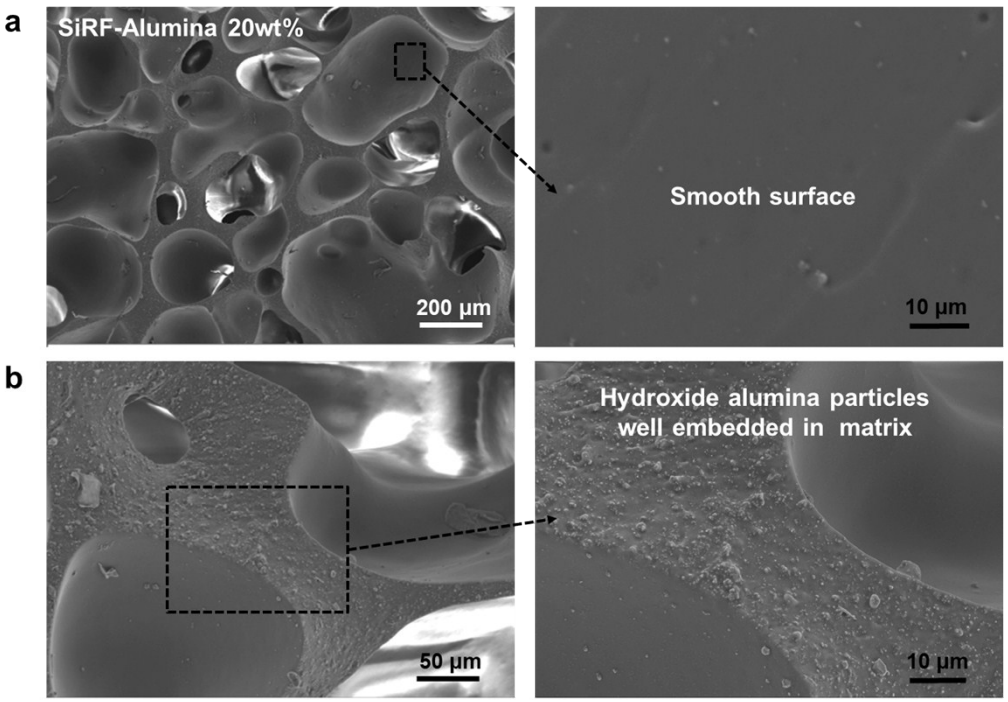

Fig. S12. Morphology of SiRF composites with 20 wt.% traditional flame retardants of hydroxide aluminium particles. (a) Surface and (b) SEM image of fractured composites, showing smooth surface and highly dispersed particles.

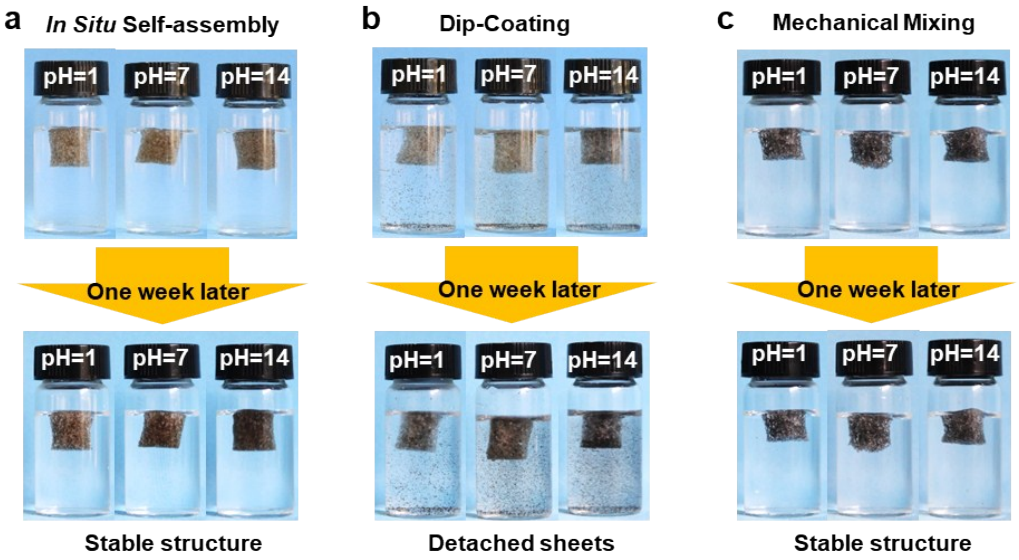

Fig. S13. Photographs of different SiRF-GO nanocomposite samples squeezed into aqueous solution at different pH values before/after 7 days. Three types of SiRF-GO nanocomposites fabricated by (a) *in-situ* self-assembly, (b) dip-coting process and (c) mechanical mixing procedure. The samples were squeezed into the solution and observed after 7 days.

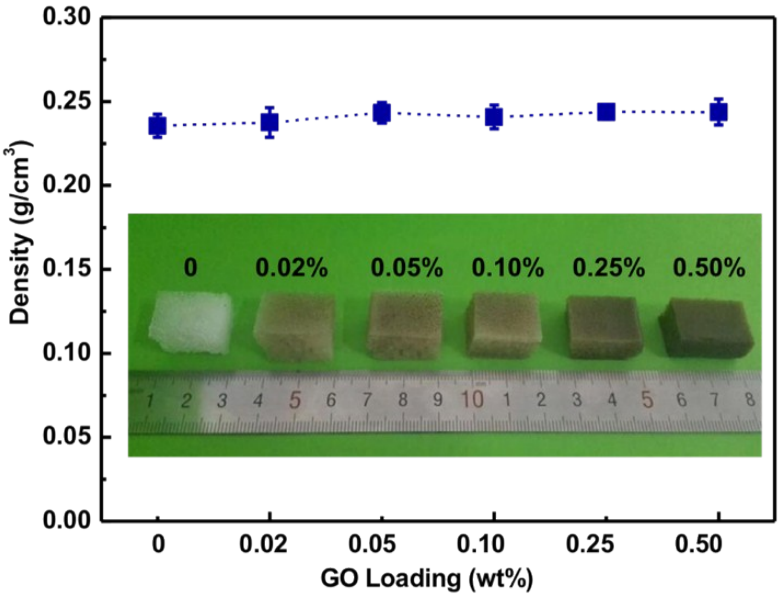

Fig. S14. Density of pure SiRF and SiRF-GO nanocomposites plotted as a function of GO loading. (Inset gives photos of SiRF samples). Clearly, the density is almost unchanged after *in-situ* assembly of ultralow GO sheets (<0.50 wt.%).

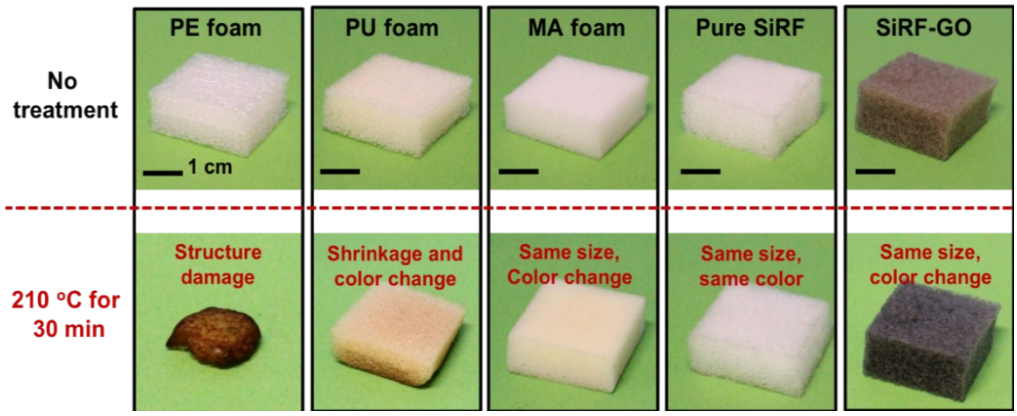

Fig. S15. Comparisons of the structural stability of traditional hydrocarbon polymer foams (i.e., polyethylene (PE) and PU), melamine (MA) foam, pure SiRF and SiRF-GO0.10% after 210 °C treatment for 30 min. Generally, traditional polymers are sensitive to environmental temperature, and after 210 °C treatment for 30 min, obvious collapse of PE or PU foams and obvious white-turning-yellow phenomenon for the flame-retardant melamine foam can be seen. However, SiRF-GO nanocomposites show excellent high-temperature resilience and structural stability after 210 °C treatment for 30 min.

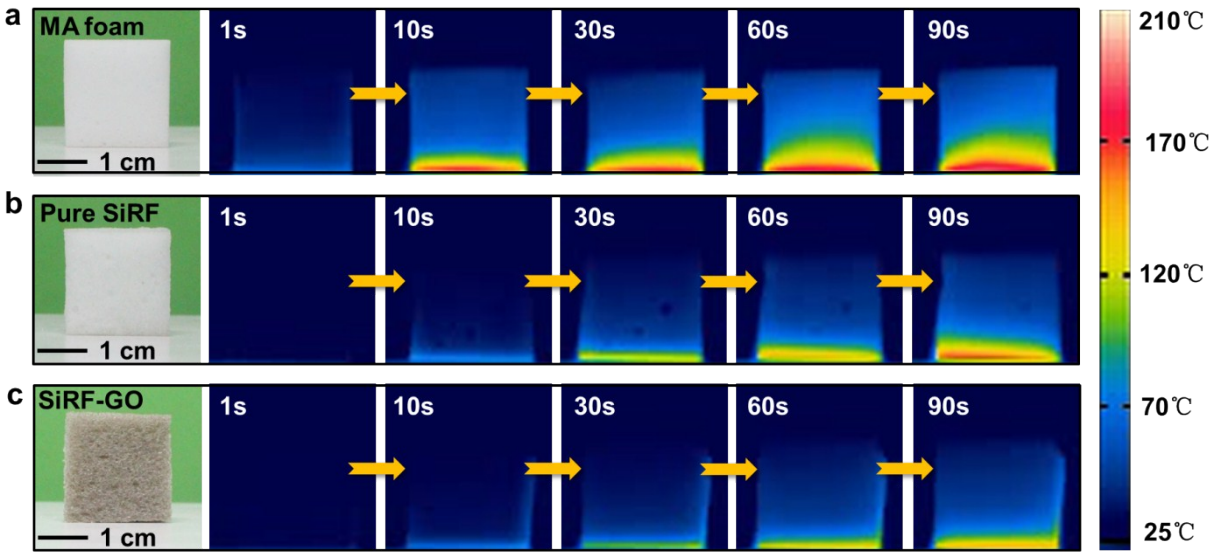

Fig. S16. Thermographic images of (a) melamine (MA) foam, (b) pure SiRF and (c) SiRF-GO0.10% samples oriented normal to the heat source of 210 ^{o}C. The colors in the thermographic images show the temperature distribution on the surface of the foams. The temperature of heated surface was ~210 ^{o}C, and the thermographic image was observed after putting the sample on the heated surface for 90 s. Thermographic recordings illustrate heat transport seems to be suppressed more in the radial direction of the SiRF-GO0.10% sample compared with the pure SiRF and MA foam.

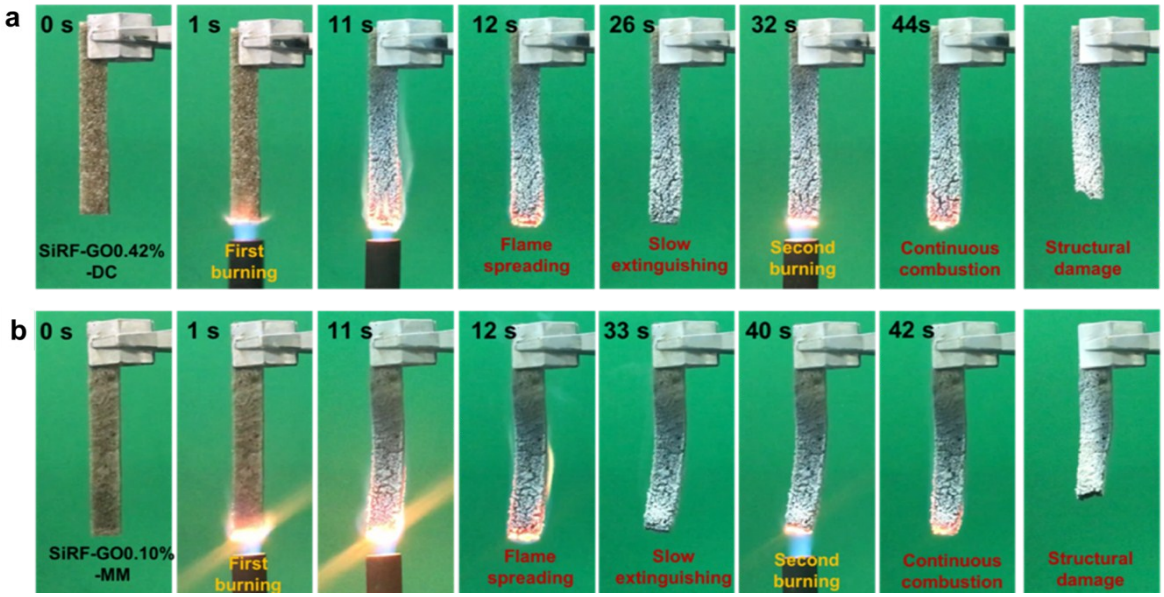

Fig. S17. Photographs of vertical burning tests of two types of SiRF-GO nanocomposites: (a) dip-coating (DC) process and (b) mechanical mixing (MM) procedure. Clearly, the SiRF-GO0.42%-DC and SiRF-GO0.10%-MM nanocomposites display slight flame spreading and structure damage during the burning tests.

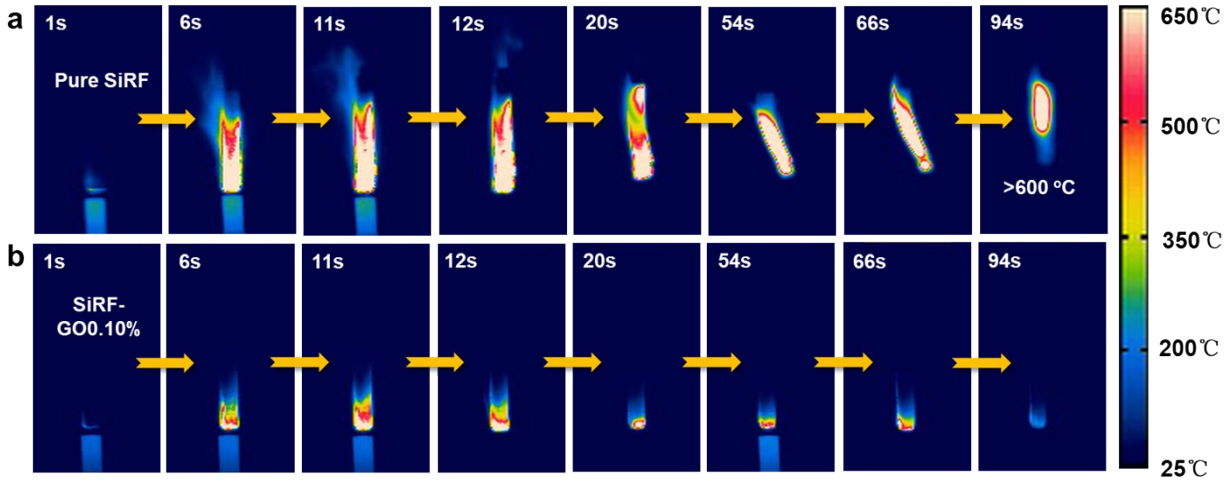

Fig. S18. Thermographic images of (a) pure SiRF and (b) SiRF-GO0.10% samples during the burning tests. Pure SiRF can be easily ignited due to the high flame temperature of ～1000 °C for an alcohol blast burner and the low ignition temperature of the PDMS molecules; and the endothermic pyrolysis of the SiRF materials produces vaporization of decomposed products and releases the effective heat flux, thus resulting in rapid flame spread and finally causing structural damage. By contrast, the presence of an ultrathin GO coating (SiRF-GO0.10%) produces slight combustion after the ignition process, and, more importantly, when removing the flame at 12 s the flame does not spread to the upper sample and can be rapidly self-extinguished in several seconds. After applying the second burning process for 10 s, the flame zone SiRF-GO0.10% displays much lower temperature and smaller zone compared with those after the first burning. The temperature in the flame zone gradually decreases and finally extinguishes the flame, which does not damage the structural integrity.

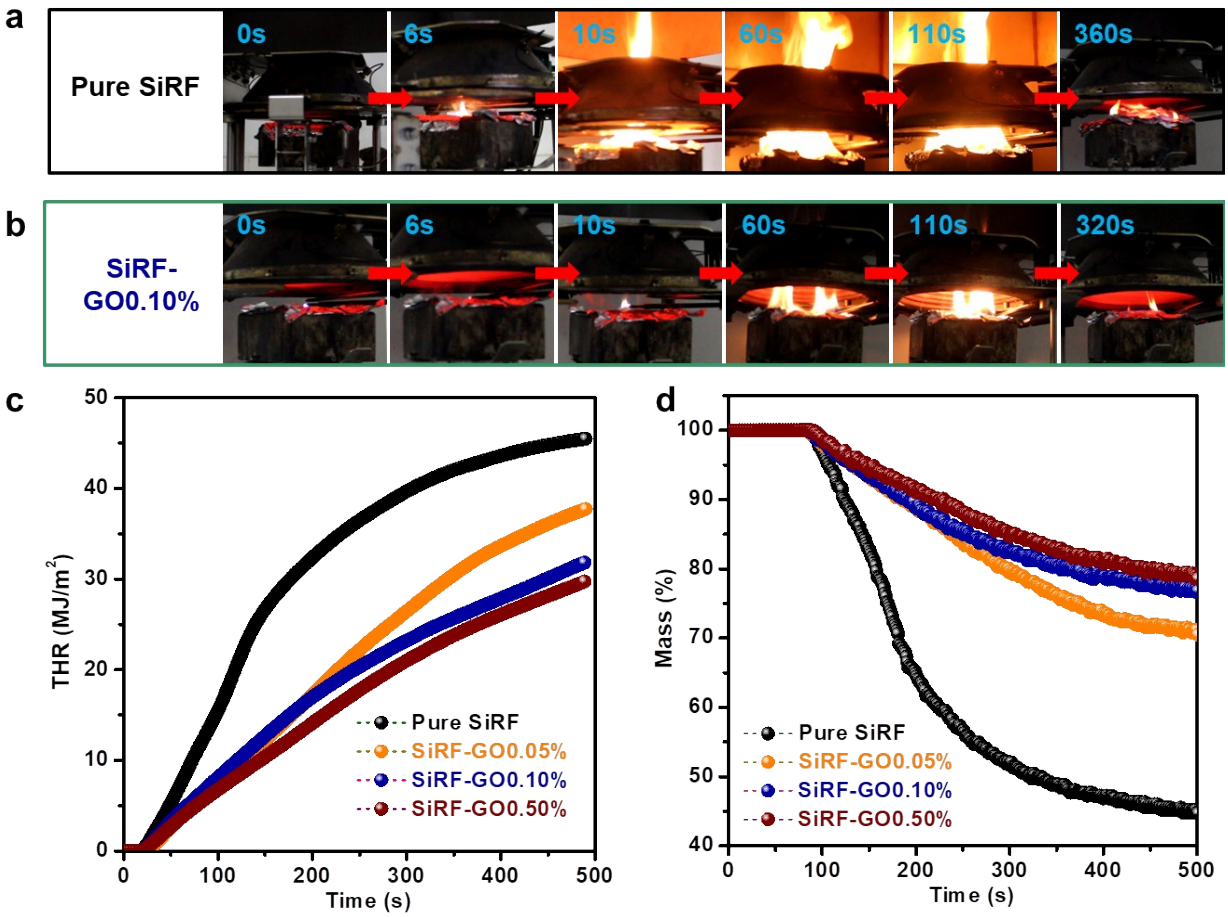

Fig. S19. Cone calorimetry tests and results of pure SiRF and SiRF-GO nanocomposites. Combustion processes of (a) pure SiRF and (b) SiRF-GO0.10%, respectively. (c) Total heat release (THR), and (d) mass change of different samples as a function of time.

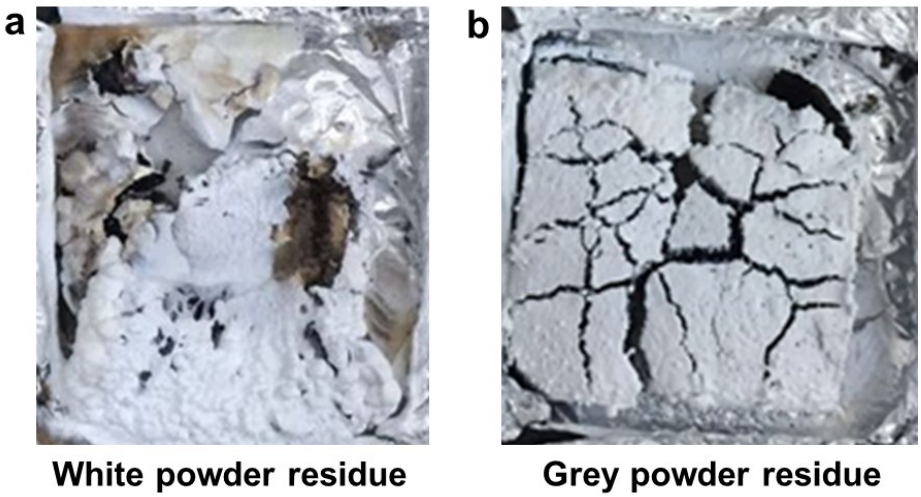

Fig. S20. Residues after cone calorimetry tests. Residue photographs of (a) pure SiRF and (b) SiRF-GO0.10% after burring tests. The pure SiRF shows an incomplete white powder residue, while the SiRF-GO0.10% displays a relatively complete and grey residue.

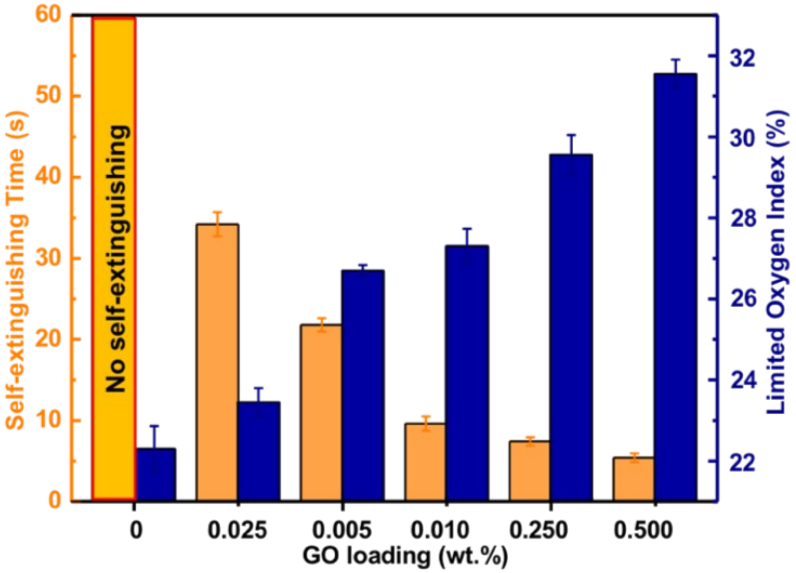

Fig. S21. Self-extinguishing time and limited oxygen index (LOI) of SiRF-GO composites as a function of GO loading.

Fig. S22. Typical digital images of different SiRF samples at a fixed oxygen concertation of 27% in the container: (A) pure SiRF, (B) SiRF-GO0.10% prepared by the *in-situ* reactive assembly (IRSA) approach, (C) SiRF-GO0.42% prepared by the DC approach, and (D) SiRF-GO0.10% prepared by the MM approach. Clearly, SiRF-GO0.10% sample containing *in-situ* assembled GO sheets shows better flame resistance compared to SiRF samples prepared by traditional DC or MM method although the GO content is almost same.

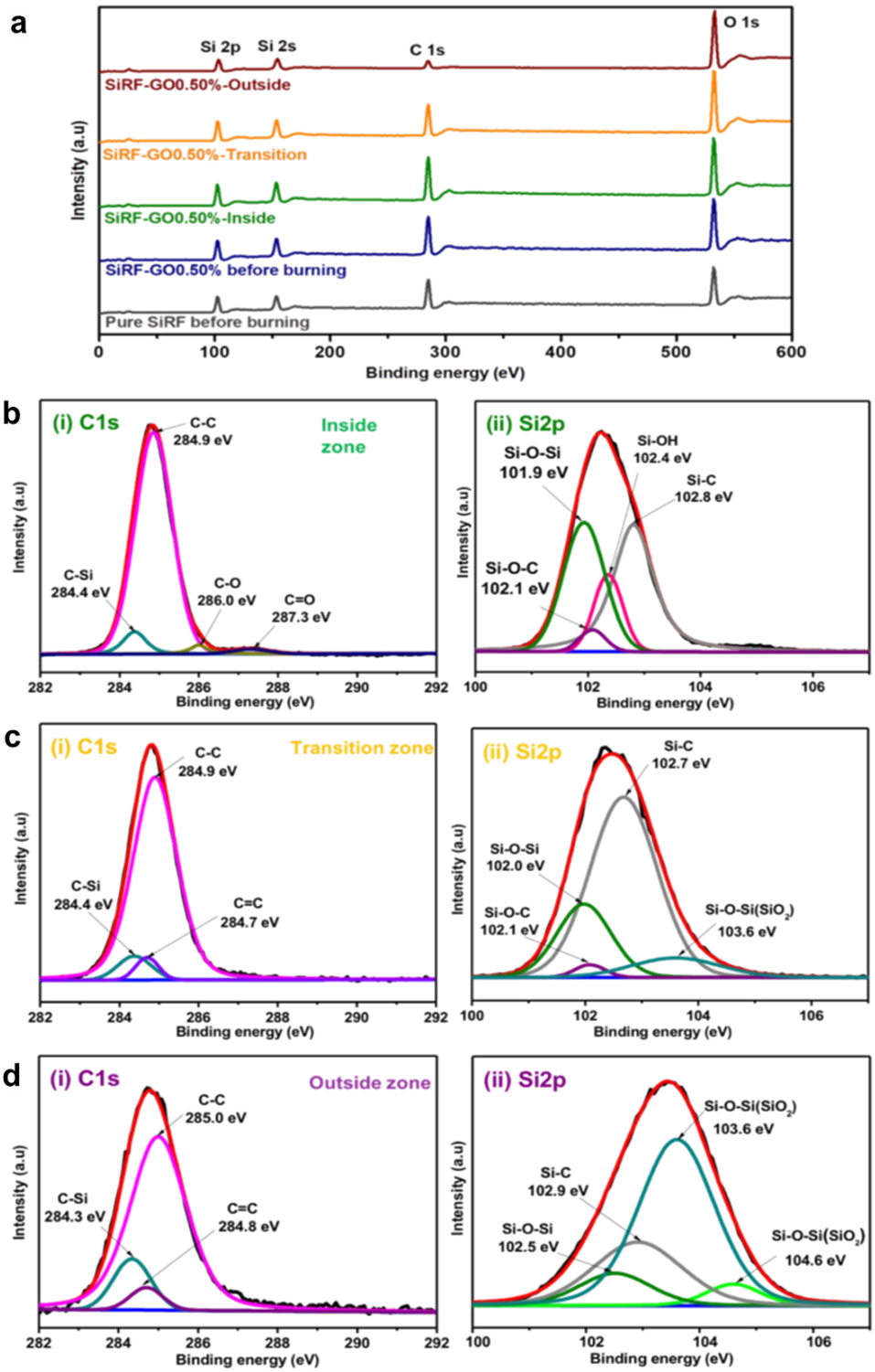

Fig. S23. (a) XPS results of pure SiRF and SiRF-GO0.10% nanocomposites before and after combustion. C1s and Si2p spectra of SiRF-GO0.10% nanocomposites observed at different zones: (b) inside zone, (c) transition zone and (d) outside zone. Compared with pure SiRF, SiRF-GO0.50% shows a slight increase in C/O ratio and the presence of Si-O-C bonding energy can be observed in both the inside and transition zones, further demonstrating the effective chemical bonds between the GO and the PDMS molecules.

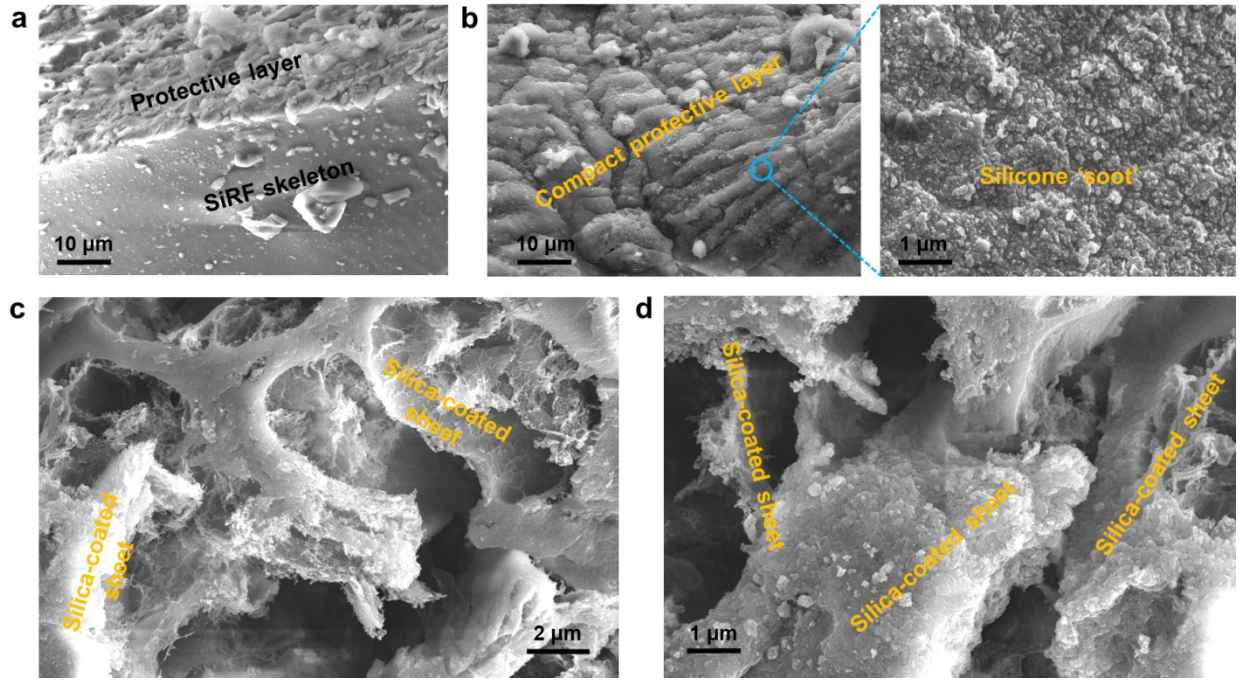

Fig. S24. Morphology and structure of SiRF-GO0.50% nanocomposites after combustion. SEM images of the nanocomposites in the outside zone: (a, b) compact protective layer and (c, d) typical silica-coated RGO sheets. Formation of the compact silicone soot on the surface can effectively protect the inside silicone molecules; and many silica nanoparticles can be observed to be adhered onto the RGO sheet surface due to the complex chemical reactions during burning.

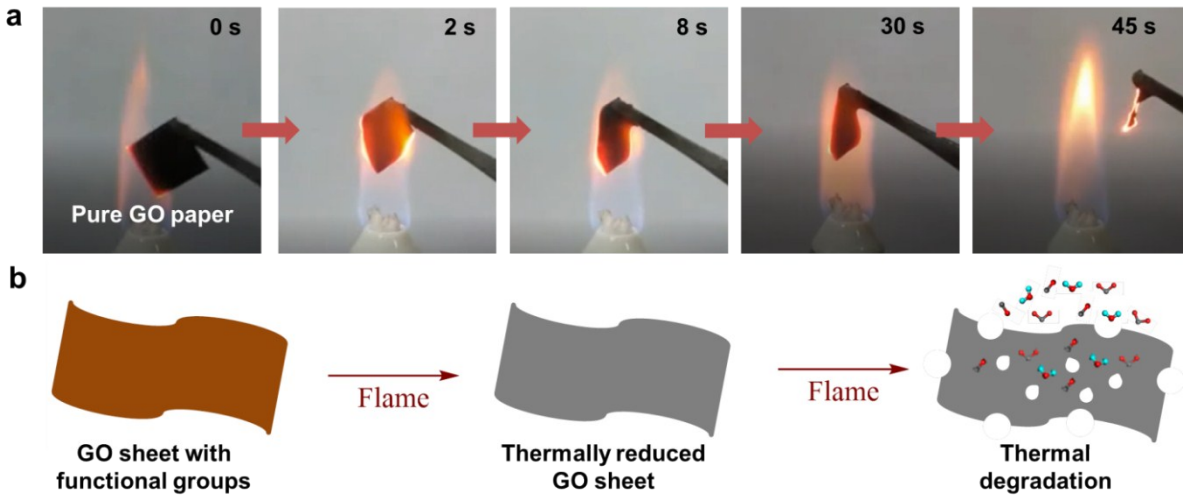

Fig. S25. Combustion process of pure GO paper. (A) Photographs of burning of pure GO paper on ethanol flame, showing complete thermal degradation in 45 s. (B) Schematic illustration of the thermal degradation of GO paper.

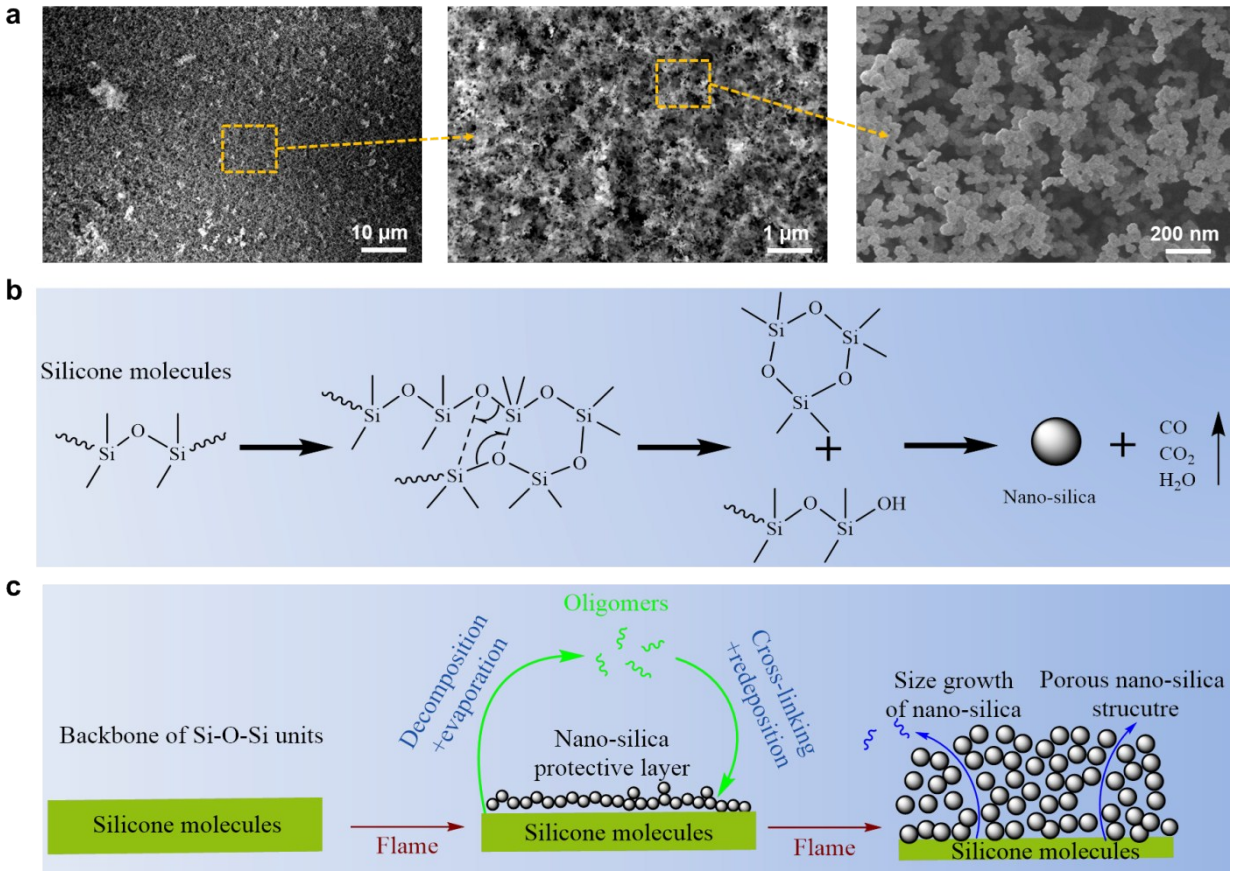

Fig. S26. Morphological and structural analyses of pure SiRF. (A) SEM images of pure SiRF after burning, showing the porous nano-silica structure. (B) Schematic illustration of thermal degradation of silicone molecules and (C) formation of porous nano-silica structure. During the flaming process, thermal degradation of silicone molecules includes the depolymerization of Si-O backbone, decomposition of organic side groups, and crosslinking. Thus, the oligomers occur during evaporation and re-deposition in the form of silicone soot in a high-temperature environment, leading to the formation of the porous nano-silica structure on the surface.

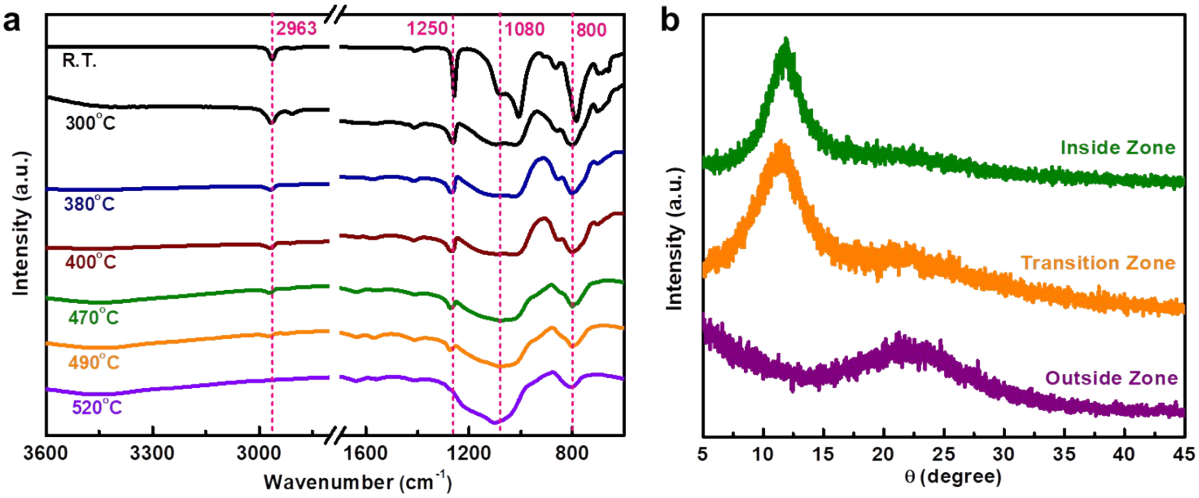

Fig. S27. Characterization of SiRF-GO nanocomposites under different temperature conditions and burnt zones. (a) FTIR results of SiRF-GO0.10% nanocomposites after different high-temperature treatment. (b) XRD results of SiRF-GO0.50% nanocomposites observed at different zones.

Table S1. Analysis of TGA results of pure SiRF and SiRF-GO nanocomposites.

Sample	$T_{5\%}$ (°C)	T_{max} (°C)	*dW/dTmax* (%/°C)	Residue (%)
Pure SiRF	336	351	0.81	61.3
SiRF-GO0.05%	348	356	0.64	68.8
SiRF-GO0.10%	352	361	0.52	69.4
SiRF-GO0.25%	357	365	0.49	69.7

$T_{5\%}$: temperature of 5% weight loss; T_{max}: temperature of maximum loss of weight; Residue was measured at ~780 °C from Fig. 3C.

Table S2. Multi-layered flame-retardant coatings on various combustible substrates through LbL or other coating techniques.

Coating composition	Substrate matrix	Fraction (wt.%)	Number of coating	Thickness of coating (nm)	Reference
PSP/PAAm (BPEI)	Cotton fabric	17.5	40	500	[2]
PEI/MMT/PAA	PU foam	3.18	24	1000±450	[3]
CH/MMT	PU foam	4.01	20	69.8	[4]
PAA/BPEI/MMT	PU foam	4.8	9	344±20	[5]
Graphene/phosphonic acid	Hanji paper	13.6	>3	--	[6]
F-POSS/APP/bPEI	Cotton fabric	--	3	246±54	[7]
Porous alginate/clay	PU foam	15	1	10000-30000	[8]
Cellulose/MMT	Textile	5	1	8500±3000	[9]
PVA cross-linked MMT	PET film or PU foam	--	213±7	625±20	[10]
CH/APP	SiRF	2.4	14	--	[11]
CH/MMT	SiRF	4.1	14	--	[11]
Silicone resin	PU foam	480	1	--	[12]
CH/GO	PU foam	13.4	12	~400	[13]
Silicone/GO	PU foam	190	3	600-800	[14]
PDA/GO	PU foam	5.0	1	>80	[15]
GO	***SiRF***	***0.10***	***--***	***~6***	***This work***

PVA: polyvinyl alcohol; **MMT**: montmorillonite; **PET**: polyethylene terephthalate; **PU**: polyurethane; **PAA**: poly(acrylicacid); **PEI**: polyethylenimine; **PSP**: poly(sodiumphosphate); **PAAm**: poly(allylamine); **BPEI**: branched polyethylenimine; **CH**: chitosan; **PDA**: polydopamine.

Table S3. Experimental results of cone calorimetry tests of pure SiRF and SiRF-GO nanocomposites.

Sample	pHRR (kW/m^2)	THR (MJ/m^2)	TSP (m^2)	Residue (%)
Pure SiRF	267.2	45.5	13.4	42.7
SiRF-GO0.05%	117.3	37.7	2.9	69.6
SiRF-GO0.10%	114.0	31.8	1.7	74.5
SiRF-GO0.50%	96.9	29.7	1.8	76.8

pHRR: peak of heat release rate; **THR**: total hear rate; **TSP**: total smoke production.

Table S4. LOI values and UL-94 results of pure SiRF and SiRF-GO nanocomposites.

Sample	LOI（%）	UL-94
Pure SiRF	22.3±0.6	NR
SiRF-GO0.02%	23.5±0.4	NR
SiRF-GO0.05%	26.7±0.1	V1
SiRF-GO0.10%	27.3±0.4	V0
SiRF-GO0.25%	29.6±0.5	V0
SiRF-GO0.50%	31.6±0.4	V0

LOI: limited oxygen index.

Table S5. Comparisons of processing, relative density and flame-retardant properties of SiRF-GO (this work) with published studies.

Filler type	Fraction (wt%)	Processing	Density (%)	LOI value (%)	PHRR (kW/m²)	UL-94 test	Reference
No	0	Mechanical mixing	480	--	74	--	[16]
MH	11		660	--	78	--	
MH:ZB(10:1)	11		710	--	82	--	
MH:ZB(6:5)	11		650	--	84	--	
MH:anhZB(10:1)	11		600		76		
MH:anhZB(6:5)	11		590		76		
No	0	Mechanical mixing	197	20.5	--	NC	[17]
CNT	0.1		258	22.0	--	NC	
	0.5		272	27.1	--	NC	
	1.0		291	30.0	--	V2	
No	0	Mechanical mixing	280	21.3	--	NC	[18]
Melamine	~10		320	25.7	--	V1	
Melamine+Graphite	~20		360	41.1	--	V0	
No	0	Layer-by-Layer assembly	180	20.2	208.6	--	[11]
CH/APP	2.4		184	23.8	151.0	--	
	3.6		186	24.3	152.9	--	
	7.5		194	24.8	194.9	--	
CH/MMT	4.1		187	23.4	169.8	--	
	6.8		192	24.7	150.6	--	
	13.2		204	25.7	149.8	--	
No	0	Extrusion and	810	--	--	NC	[19]
Lignin	25		650	--	--	--	

	41[b]		600	--	--	NC	
	41[c]		--	--	--	V0	
No	0	Mechanical mixing (A foaming agent)		22.0	241.20	--	[20]
Functionalized GO	0.5			23.4	185.53	--	
	1.0			24.4	165.98	--	
	3.0			25.4	135.58		
	5.0			27.6	122.47	--	
No	0	--	235	22.3	267.2	NC[a]	***This work***
	0.10	Mechanical mixing	235	--	--	NC[a]	
	0.42	Dip-coating	235	--	--	NC[a]	
GO	*0.05*	*In-situ reactive assembly*	*237*	*26.7*	*118.6*	*V1*	
	0.10		*243*	*27.3*	*117.3*	*V0*	
	0.50		*244*	*31.6*	*96.9*	*V0*	

MH: Magnesium hydroxide; **ZB**: Zinc borate; **anhZB:** Firebrake 500 ZB; **CNT**: carbon nanotube.

T_{d5}: temperature of 5 % weight loss of TGA; **PHHR**: peak heat release rate; **LOI**: limited oxygen index.

[a] **NC**: not classified; [b]: no thermal/NH_3 vapor post-treatment applied; [c]: thermal/NH_3 vapor post-treatment applied.

Table S6. XPS element analysis of pure SiRF and SiRF-GO0.50% nanocomposites.

Sample	C (wt%)	Si (wt%)	O (wt%)
Pure SiRF	48.04	26.40	25.56
SiRF-GO0.50%	48.47	25.71	25.82
Inside zone	48.66	25.68	25.67
Transition zone	39.98	27.17	32.85
Outside zone	17.91	29.66	52.43

Table S7. C1s XPS spectra of pure SiRF and SiRF-GO0.50% nanocomposites.

Sample	C1s fitting binding energy (eV; relative atomic percentage, %)				
	C-Si	C-C	C-O	C=O	C=C
Pure SiRF	10.3	89.7	--	--	--
SiRF-GO0.50%	13.5	80.8	3.5	2.2	--
Inside zone	6.7	89.1	2.4	1.8	--
Transition zone	7.2	88.2	--	--	4.6
Outside zone	13.7	81.1	--	--	5.2

Table S8. Si2p XPS spectra of pure SiRF and SiRF-GO0.50% nanocomposites.

Sample	Si2p fitting binding energy (eV; relative atomic percentage, %)					
	Si-O-Si	Si-O-C	Si-OH	Si-C	Si-O-$Si(SiO2)_1$	Si-O-$Si(SiO2)_2$
Pure SiRF	32.2	--	21.2	46.6	--	--
SiRF-GO0.50%	36.0	3.2	14.5	46.3	--	--
Inside zone	36.2	3.8	14.9	45.1	--	--
Transition zone	22.1	2.1	--	66.3	9.5	--
Outside zone	10.7	--	--	25.8	58.1	5.4

Movie S1. Burning processes of polyurethane (PU) and melamine (MA) foams. In an alcohol blast burner, PU foam can be easily ignited and shows rapid and complete combustion with serious smoke release. Comparatively, MA foam can be burnt down in 10 s although the foam shows self-extinguishing behavior. (Play speed: x1)

Movie S2. Burning process of pure SiRF. Upon burning in an alcohol blast burner, pure SiRF can be ignited in 10 s, and the flame spreads to the whole sample and finally induces complete combustion and serious structural damage. (Play speed: x4)

Movie S3. Burning process of SiRF-GO0.10% nanocompsoites prepared by the IRSA approach. Upon burning in an alcohol blast burner, SiRF-GO0.10% prepared by the IRSA approach shows excellent flame resistance and rapid self-extinguishing even twice after 10 s burning. The flame does not spread, and the structural integrity can be well kept. (Play speed: x4)

References

[1] S. Xiaoming, L. Dachao, L. Junfeng, D. G. Evans, *ACS. Nano.* **2010**, *4*, 3381.

[2] Y.-C. Li, S. Mannen, A. B. Morgan, S. Chang, Y.-H. Yang, B. Condon, J. C. Grunlan, *Adv. Mater.* **2011**, *23*, 3926.

[3] Y. S. Kim, R. Harris, R. Davis, *ACS Macro Letters* **2012**, *1*, 820.

[4] G. Laufer, C. Kirkland, A. A. Cain, J. C. Grunlan, *ACS Appl. Mat. Inter.* **2012**, *4*, 1643.

[5] Y. C. Li, Y. S. Kim, J. Shields, R. Davis, *J. Mater. Chem. A* **2013**, *1*, 12987.

[6] M.-J. Kim, I.-Y. Jeon, J.-M. Seo, L. Dai, J.-B. Baek, *ACS. Nano.* **2014**, *8*, 2820.

[7] S. Chen, X. Li, Y. Li, J. Sun, *ACS. Nano.* **2015**, *9*, 4070.

[8] H. B. Chen, P. Shen, M. J. Chen, H. B. Zhao, D. A. Schiraldi, *ACS. Appl. Mater. Inter.* **2016**, *8*, 32557.

[9] P. Das, H. Thomas, M. Moeller, A. Walther, *Sci. Rep.* **2017**, *7*, 39910.

[10] F. Ding, J. Liu, S. Zeng, Y. Xia, K. M. Wells, M.-P. Nieh, L. Sun, *Sci. Adv.* **2017**, *3*, e1701212.

[11] S. B. Deng, W. Liao, J. C. Yang, Z. Cao, Y. Z. Wang, *Ind. Eng. Chem. Res.* **2016**, *55*.

[12] Q. Wu, Q. Zhang, L. Zhao, S.-N. Li, L.-B. Wu, J.-X. Jiang, L.-C. Tang, *J. Hazard. Mater.* **2017**, *336*, 222.

[13] L. Maddalena, F. Carosio, J. Gomez, G. Saracco, A. Fina, *Polym. Degrad. Stab.* **2018**, *152*, 1.

[14] Q. Wu, L.-X. Gong, Y. Li, C.-F. Cao, L.-C. Tang, L. Wu, L. Zhao, G.-D. Zhang, S.-N. Li, J. Gao, Y. Li, Y.-W. Mai, *ACS. Nano.* **2018**, *12*, 416.

[15] Hanim Kim, Dae Woo Kim, Vivek Vasagar, Heonjoo Ha, Sergei Nazarenko, C. J. Ellison, *Adv. Funct. Mater.* **2018**, *28*, 1803172.

[16] A. Genovese, R. A. Shanks, *Compos. Part. A.* **2008**, *39*, 398.

[17] R. Verdejo, F. Barroso-Bujans, M. A. Rodriguez-Perez, J. A. de Saja, M. Arroyo, M. A. Lopez-Manchado, *J. Mater. Chem.* **2008**, *18*, 3933.

[18] J. J. Chrusciel, E. Lesniak, *J. Appl. Polym. Sci.* **2011**, *119*, 1696.

[19] J. Zhang, E. Fleury, Y. Chen, M. A. Brook, *RSC Adv.* **2015**, *5*, 103907.

[20] T. Xu, C. Zhang, P. Li, X. Dai, L. Qu, Y. Sui, J. Gu, Y. Dou, *New J. Chem.* **2018**, *42*, 13873.